



**POLITECNICO**  
**MILANO 1863**

**SCUOLA DI INGEGNERIA INDUSTRIALE  
E DELL'INFORMAZIONE**

EXECUTIVE SUMMARY OF THE THESIS

## Numerical study of the impact of nozzle shape on underexpanded jet - wall interaction.

LAUREA MAGISTRALE IN AERONAUTICAL ENGINEERING - INGEGNERIA AERONAUTICA

**Author:** ROBERTO D'ANGELO

**Advisor:** PROF. LUIGI VIGEVANO

**Co-advisor:** PROF. KOEN HILLEWAERT (ULIÈGE)

**Academic year:** 2021-2022

---

### 1. Introduction

Supersonic jet impingement has a practical importance in many engineering fields, such as control of heat transfer, STOVL aircraft hovering near the ground, launching and landing of aircraft and spacecraft, among others. For this reason, jet impingement has been extensively investigated throughout the years. Nevertheless, some important aspects are still ill-known nowadays. In fact, this kind of flow is rather complex as it includes many different flow features, such as: coexistence of subsonic and supersonic regions, shock interactions, stand-off shocks, recirculation regions, among the others. Furthermore, their behavior is dependent on a wide range of parameters, such as stage of underexpansion (moderately or highly underexpanded) and nozzle-to-wall distance, among others.

In this framework, this work inscribes itself in a joint effort between the laboratory André Jaumotte of the Université Libre de Bruxelles and the University of Liège, aiming to develop an experimental setup to further investigate the ground effect on a small scale. In particular, this work aims to numerically investigate if the free-flow and impinging-flow structures are affected by the nozzle geometry, and if yes, to what ex-

tent. This is accomplished by considering three different nozzles: one contoured and two conical nozzles with different lengths. Shape and dimension of the nozzles are chosen accordingly to previous computations performed at the above-mentioned laboratory. To cover a wider range of configuration, the nozzle-pressure-ratio (NPR) and the nozzle-to-plate distance are also varied. The focus is specifically placed on axisymmetric underexpanded turbulent jets impacting on a flat plate. In particular, the steady state of the supersonic impingement will be analysed.

### 2. Numerical Method

The study hereafter reported is performed exploiting the in-built axisymmetric solver of the open-source CFD code SU2. In particular, a numerical investigation concerning axisymmetric underexpanded turbulent jets issuing from a convergent-divergent nozzle is carried out by means of Reynolds averaged Navier-Stokes (RANS) equations. To assess the most suitable turbulence model for these kinds of simulations, the Spalart-Allmaras (SA) and the Menter Shear Stress Transport (SST) are tested and discussed in Section 3.

The fluid is modelled as perfect gas. The numer-

ical method is a *Finite Volume Method*, while the numerical schemes chosen are the *Roe* solver for the convective fluxes and the *Green-Gauss* method to compute the gradients. Second order accuracy is achieved via reconstruction of variables on the cell interfaces by using a *Monotone Upstream-Centered Scheme for Conservation Laws* approach. The use of gradient limiters is necessary for these kinds of simulations and hence the Venkatakrisnan is employed. A damped inexact Newton iteration is used for the equations time-stepping. The corresponding linear system is solved using the *Flexible Generalized Minimal Residual* method.

Regarding the computational domain, the axisymmetric solver allows the use of two-dimensional grids to solve an axisymmetric three-dimensional problem. The grids are unstructured and finer where high flow gradients are expected, i.e. in the region of the free expansion of the jet and, in case of impingement configuration, above the impinged wall.

To perform numerical simulations of high-quality grids, the NIC5 High Performance Computing (HPC) cluster on the University of Liège has been exploited.

### 3. Validation and Verification

Validation and Verification are performed in order to demonstrate the accuracy of the numerical method and assess credibility of extrapolated data in the following analysis.

The governing equations are supposed to be correctly implemented, hence in this work verification only consists of proving simulation independence from the grid. The number of cells which ensures grid independence is dependent on the computational domain extension and spans from  $\sim 700.000$  (impinging case) to over 1.100.000 (free jet case).

The numerical method is validated against available experimental data found in open literature. For the free-jet case the computational parameters are summarized in Table 1 and refer to the experimental set-up of Troutt and McLaughlin [1], which employed a convergent-divergent nozzle of outer diameter  $D_e = 10\text{mm}$  to accelerate a flow to a moderately underexpanded jet issuing in a quiescent environment at low ambient pressure  $P_\infty = 5000\text{Pa}$ .

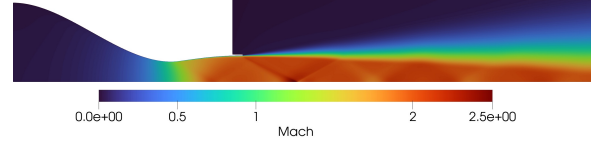


Figure 1: Colour plot of the Mach number in case of computational parameters of Table 1.

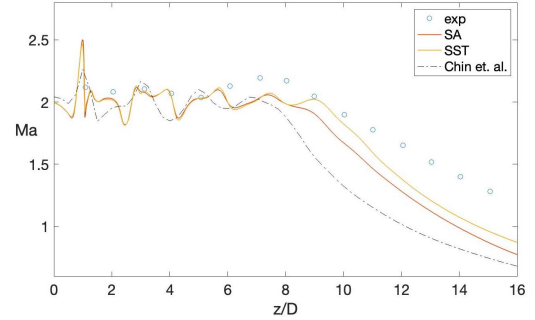


Figure 2: Axial Mach number per different turbulence models compared with results of [1, 2].

$M_e$	$Re_e$	$P_e/P_\infty$	$D_e$	$A_e/A_t$
2	$5 \times 10^4$	1.03	10mm	1.6875

Table 1: Computational parameters in case of free jet. The subscript  $e$  refers to the nozzle exit section, while  $t$  to the throat.

Figure 2 reports the results obtained for the Mach number evolution along the domain centre-line for different turbulence models (SA and SST). The results are also compared with the experimental measurements obtained in [1] and the numerical solution of [2]. Some divergences between the numerical simulations and the experimental data can be acknowledged. First of all, the wide oscillations predicted are due to the quasi-periodic "diamond" structures present in the free-jet evolution. Also, substantial differences from reality are predicted in the farfield region ( $z/D > 8$ ) due to the decay of flow characteristics which is intrinsic in the turbulence modeling. Nevertheless, the results compare well with the references, especially at short distances from the nozzle outlet ( $z/D < 6$ ).

Similar conclusions can be made referring to the Mach number profiles in radial direction, reported for axial distances from the nozzle outlet  $z/D = [1, 5]$  in Figure 3. Results forecast almost coincident behavior of experimental

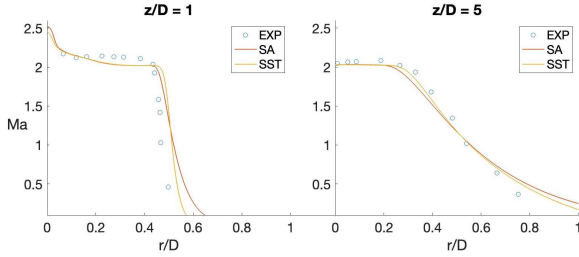


Figure 3: Comparison of the streamwise Mach number profiles in the radial direction at axial location  $z/D = 1$  (left) and  $z/D = 5$  (right) obtained with different turbulence models. The results are compared with the experimental data reported in Troutt and McLaughlin [1].

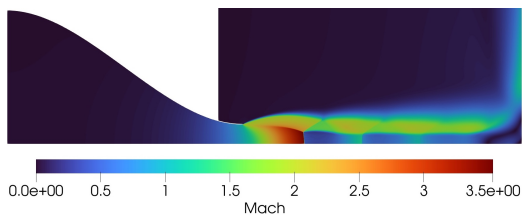


Figure 4: Colour plot of the Mach number in case of computational parameters of Table 2.

data, confirming that the core region of the flow is correctly predicted by both the turbulence models. On the other hand, at further distances the decay of the characteristic plays once again a major role in underestimating the velocity. In this phase, overall good agreement with real data is shown for the near-flow region ( $z/D < 6$ ), which is the area of interest of this work. Additionally, for the moderately underexpanded free-jet, the SST showed slightly better performance than the SA in replicating the experimental data.

$M_e$	$Re_e$	$P_e/P_\infty$	$D_e$ [mm]	$z/D$
1	$1.3 \times 10^6$	3.57	13.3	7.3, 23.5

Table 2: Computational parameters in case of impinging jet. The subscript  $e$  refers to the nozzle exit section.

Next the impinging-jet configuration is analysed. The computational parameters are reported in Table 2. The reference in this case is the experimental measurements performed by Donaldson and Snedeker [3], which tested

a highly underexpanded jet generated by a purely convergent nozzle of outer diameter  $D = 13.26\text{mm}$  exhausting to atmospheric pressure  $P_\infty$ . The different nozzle size implies modifying the existing computational domain size and grid resolution to ensure the same accuracy in results as in the free-jet case. This is accomplished by scaling the average cells size accordingly to the throat radius ratio of the two cases. Additionally, the boundary conditions must be changed to match the experimental parameters.

Results for the pressure distributions over the wall are reported for distance  $z/D = 7.3$  in Figure 5. The numerical method shows capability in predicting the occurrence of a recirculation region, indicated in Figure 5 by the presence of an off-axis peak in pressure. To some extent, overall good agreement in the pressure pattern and location of the pressure peak are also recognised. The pressure is overestimated for distances beyond the aforementioned pressure peak once again due to turbulence modeling. Furthermore, the numerical results compare well with numerical data of [2] for distance  $z/D = 23.5$  shown in Figure 6, as well as with experimental data of [3]. Finally, the positioning of the first Mach disk is hereby predicted with an accuracy of 97.5% (same results for both the wall distances).

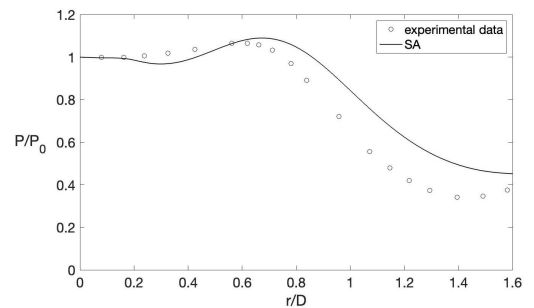


Figure 5: Comparison of stagnation region pressure distribution over the plate with the experimental results of [3], where the reference pressure  $P_0$  is the center-line stagnation pressure over the plate.

It must be noted that for a highly underexpanded impinging jet the results are reported only for the SA turbulence model. In fact, the SST failed to predict the behavior of the flow field, converging to a wrong solution. In particular, the presence of a big overshoot

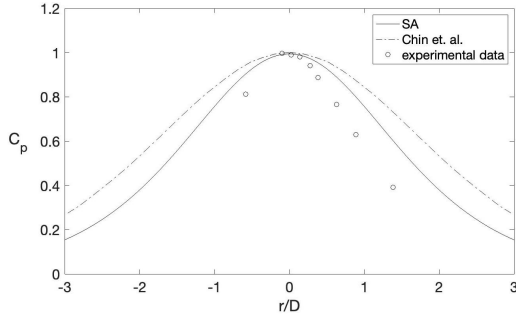


Figure 6: Comparison of the pressure coefficient distribution over the flat plate located at  $z/D = 23.5$  with the experimental results of [3] and the numerical results of [2]. The pressure coefficient is defined as  $C_p = (P - P_\infty)/(P_0 - P_\infty)$ .

in Mach number across the Mach disk and following absence of a recirculation region (for case  $z/D = 7.3$ ) have been recognised. This issue may be due to a coupling effect between strong gradients that form across normal shocks and the formulation of source terms in the SST. Indeed the latter generate eddy viscosity where velocity gradients are computed, i.e. also across normal shocks, where physically no viscous effects are expected. For this reason, the SA is considered for all the other simulations hereafter discussed.

All things considered, the numerical method appears to be able to correctly catch all the relevant flow features expected in the out-flow expansion of an underexpanded free and impinging jet, as well as providing an accurate replication of the experimental data, especially concerning the near-flow region.

## 4. Tests and Results

The final investigation is hereafter reported. As mentioned mentioned, three different convergent-divergent nozzles are employed in this phase: a contoured nozzle with exit semi-diffusive angle of  $\epsilon = 0^\circ$  (indicated as N1); a conical one with divergence section  $15\text{mm}$  long and  $\epsilon = 3^\circ$  (N2); a conical one with divergence section  $25\text{mm}$  long and  $\epsilon = 2^\circ$  (N3). The exit-to-ambient pressure ratio varies from  $P_e/P_\infty = 1.4$  (NPR1 - moderately underexpanded) to  $P_e/P_\infty = 2.5$  (NPR2 - highly underexpanded). The nozzles are fed with pressurised  $N_2$  and exhaust in a quiescent

environment at ambient pressure. Additional computational parameters are reported in Table 3.

$M_e$	$Re_e$	$P_e/P_\infty$	$D_t$	$A_e/A_t$
1.7	$1.2 \times 10^5$	[1.4, 2.5]	1mm	1.338

Table 3: Computational parameters for the final investigation. The subscript  $e$  refers to the nozzle exit section, while  $t$  refers to the throat.

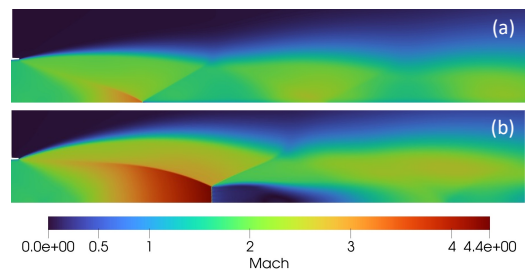


Figure 7: Mach number colour plots of the free-jet configuration for NPR1 (a) and NPR2 (b) and nozzle N2. The near-field region is magnified.

The results for the free-jet are first presented and can be seen in Figure 7 for the N2. The correspondent Mach number axial evolution is also reported in Figure 8 for all the nozzles. Some important differences in free-jet configuration can be recognised. First of all in case NPR1, different intensities of the first intercepting shock are predicted for different nozzle geometries (see

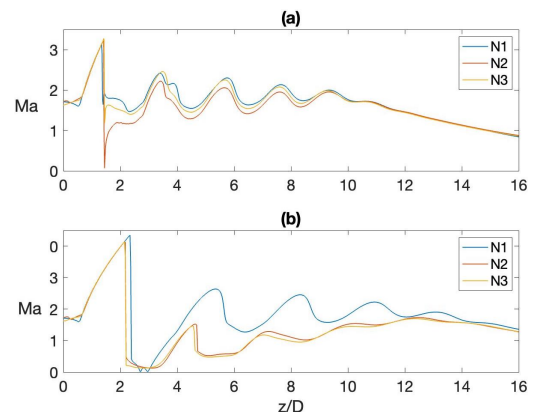


Figure 8: Mach number axial evolution of the free-jet configuration for NPR1 (a) and NPR2 (b) for different nozzle geometries.

Figure 8 (a)). In particular, the higher the nozzle divergence angle  $\epsilon$ , the higher the intensity of such shock. Moreover, for nozzle N2 ( $\epsilon = 3^\circ$ ) the formation of a small Mach disk is predicted, as proven by the subsonic value of the flow downstream the above-mentioned discontinuity. In case NPR2, the flow field presents as expected the formation of a Mach disk for all the nozzles. The diameter of such disk changes significantly with the geometry ( $D_{disk} = 0.117D$  for N1,  $D_{disk} = 0.188D$  for N2 and  $D_{disk} = 0.235D$  for N3), while its axial location is predicted almost coincident for the conical nozzles and changes within a difference of 7% for N1. The intensity of the discontinuity is in this case higher for N1 than N2 and N3. Moreover, the formation of an additional Mach disk is predicted for the conical nozzles, leading to completely different ensuing flow behavior among the three cases. Additionally, the investigation of the Mach radial profiles (for both NPR1 and NPR2) confirms different evolution of the core region and reveals that the flow differences smooth down moving radially outward. Then the curves merge, indicating that the mixing layer is not sensitive to the nozzle geometry.

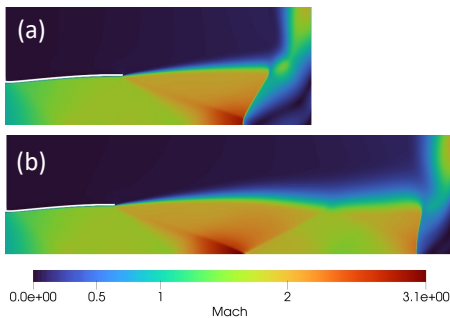


Figure 9: Mach number colour plots for nozzle N1 and NPR1 of the impinging-jet configuration for D1 (a) and D3 (b).

The impinging-jet configuration is next discussed. In this phase, the nozzle-to-wall distances tested are  $z/D = [1.8, 2.5, 3.5]$ , indicated as D1, D2 and D3, respectively. The results will nevertheless hereby be discussed only for distances D1 and D3, since discussing D2 would be redundant.

In case D1 (Figure 9, (a)) a Mach disk forms in the domain even at low exit-to-ambient pressure ratio (NPR1) due to the proximity of the wall. In this case the intercepting shock does not reflect regularly on the centre-line since it is antici-

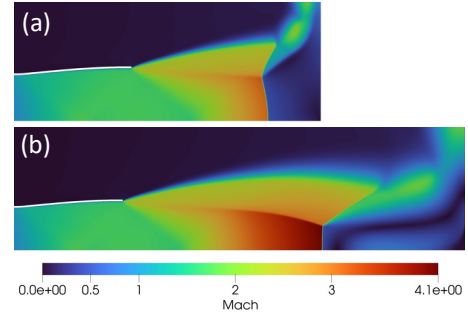


Figure 10: Mach number colour plots for nozzle N1 and NPR2 of the impinging-jet configuration for D1 (a) and D3 (b).

pated by the presence of the wall. Consequently, no relevant differences in flow evolution are recognized between the nozzles. Meanwhile in case NPR1 and D3 (Figure 9, (b)) the shock cell is fully developed and it results in a normal shock in front of the wall (plate shock) regardless of nozzle geometry. The intensity of the intercepting shock (or Mach disk for N2) is once again affected by the nozzle geometry, leading to some differences in the impingement region. In particular, the plate shock strength is the highest for N1 and the lowest for N2 (as shown in Figure 11, (a)) due to the difference in impact velocity resulting from the upstream shock. Similar conclusions can be made for the distance of the plate shock from the wall and the consequent size of the recirculation region, both influenced by the development of the first shock cell. The formation of such a recirculation region is predicted for all the distances and nozzles considered in case NPR1. The nozzle geometry is furthermore found to have a mild effect on the pressure distribution over the flat plate, shown in Figure 12. Some differences are detected at higher distances (D3), once again due to the loss introduced by the intercepting or Mach shock.

The case NPR2 is next discussed. Color plots of the Mach number are reported in Figure 10. At short nozzle-to-wall spacing (D1), the Mach disk is located at smaller axial distance compared to the free-jet, as well as enlarged in diameter. Consequently, the formation of a wide subsonic area with no recirculation bubble is predicted in this case. Furthermore, the flow behavior is rather coincident for all the nozzles in case D1 and hence is not here further detailed. On the other hand, a fully developed shock cell is formed in case D3. The flow is subsequently un-

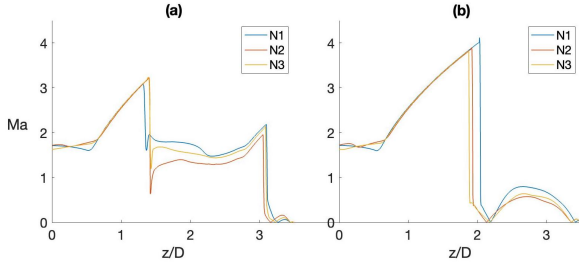


Figure 11: Mach number axial evolution of the impinging-jet configuration for NPR1 (a) and NPR2 (b) for different nozzle geometries and distance  $D3$ .

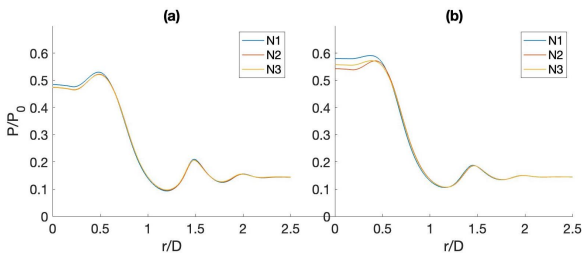


Figure 12:  $P/P_0$  distributions over the flat plate for NPR1 and for cases D1(a) and D3(b).  $P_0$  refers to the reservoir condition.

able to accelerate again to supersonic velocity, which leads to the occurrence of a recirculation bubble. The Mach disk strength is, as in the NPR2 free-jet case, the highest for nozzle N1, while it coincides for N2 and N3 (see Figure 11, (b)). This reflects evidently on the wall pressure distribution (Figure 13, (b)), which appears rather different in value for nozzle N1. Note that contrarily the pressure curves overlap each others in case D1 (Figure 13, (a)).

Finally, the radial wall-jet behavior was found to be insensitive to the nozzle geometry, regardless of distance and nozzle pressure ratio. The results are not detailed here, although it can be

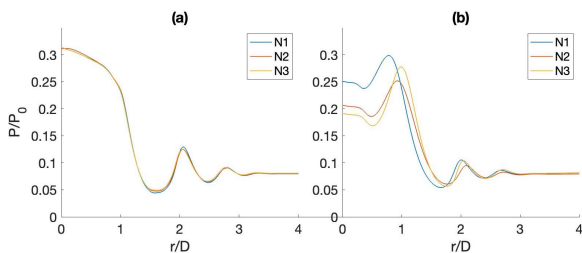


Figure 13:  $P/P_0$  distributions over the flat plate for NPR2 and for cases D1(a) and D3(b).  $P_0$  refers to the reservoir condition.

noticed that the pressure distributions generated by all the nozzles coincide at high radial coordinates for all the cases, which is per se an indication of the wall-jet behavior.

## 5. Conclusions

A numerical study on the shock structures for free and impinging underexpanded jets is carried out making use of the axisymmetric RANS solver of the CFD code SU2. Verification and validation are initially performed by proving results' independence from the employed grid and verifying the accuracy in replicating real experimental data. Results showed that the numerical set-up employed here is able to properly predict the behavior of the core region of the jet, as well as the occurrence of stagnation bubble.

The impact of the nozzle geometry on the flow field is then investigated for different operative conditions. It is found that the geometry might affect significantly the intensity of the shocks formed in the free-jet structure, resulting in different behavior in the impingement region. The discrepancies in the impinging-jet behavior are contrarily rather small when the formation of the fully developed shock cell is prevented. Finally, the jet mixing layer and radial wall-jet appear to not be sensitive to the nozzle geometry.

## References

- [1] T. R. Troutt and D. K. Mclaughlin. Experiments on the flow and acoustic properties of a moderate-reynolds-number supersonic jet. *Journal of Fluid Mechanics*, 116:123–156, 1993.
- [2] R.C. Chin, M. Li, C. Harkin, T. Rochwerger, L. Chan, A. Ooi, A. Risborg, and J. Soria. Investigation of the flow structures in supersonic free and impinging jet flows. *Journal of Fluids Engineering*, 135:031202, 2013.
- [3] C. DUP. Donaldson and R. S. Snedeker. A study of free jet impingement. part 1. mean properties of free and impinging jets. *Journal of Fluid Mechanics*, 45:281–319, 1971.